

Serveur Académique Lausannois SERVAL serval.unil.ch

Author Manuscript

Faculty of Biology and Medicine Publication

This paper has been peer-reviewed but does not include the final publisher proof-corrections or journal pagination.

Published in final edited form as:

Title: Direct in vitro comparison of six three-dimensional positive contrast methods for susceptibility marker imaging.

Authors: Vonken EJ, Schär M, Yu J, Bakker CJ, Stuber M

Journal: Journal of magnetic resonance imaging : JMRI

Year: 2013 Aug

Volume: 38

Issue: 2

Pages: 344-57

DOI: 10.1002/jmri.23976

In the absence of a copyright statement, users should assume that standard copyright protection applies, unless the article contains an explicit statement to the contrary. In case of doubt, contact the journal publisher to verify the copyright status of an article.

Published in final edited form as:

J Magn Reson Imaging. 2013 August ; 38(2): 344–357. doi:10.1002/jmri.23976.

Direct in vitro comparison of six 3D positive contrast methods for susceptibility marker imaging

Evert-jan P. A. Vonken, MD PhD^{1,2,*}, Michael Schär, PhD^{1,3}, Jing Yu, PhD¹, Chris J. G. Bakker, PhD², and Matthias Stuber, PhD^{1,4,5}

¹Russell H. Morgan Department of Radiology and Radiological Science, The Johns Hopkins University School of Medicine, Baltimore, MD ²UMC Utrecht, Department of Radiology, Utrecht, the Netherlands ³Philips Healthcare, Cleveland, OH ⁴Department of Radiology, University Hospital (CHUV) and University of Lausanne (UNIL), Switzerland ⁵Center for Biomedical Imaging (CIBM), Lausanne, Switzerland,

Abstract

Purpose—To compare different techniques for positive contrast imaging of susceptibility markers with MRI for 3D visualization. As several different techniques have been reported, the choice of the suitable method depends on its properties with regard to the amount of positive contrast and the desired background suppression, as well as other imaging constraints needed for a specific application.

Materials and methods—Six different positive contrast techniques are investigated for their ability to image at 3T a single susceptibility marker *in vitro*. The white marker method (WM), susceptibility gradient mapping (SGM), inversion recovery with on-resonant water suppression (IRON), frequency selective excitation (FSX), fast low flip-angle positive contrast SSFP (FLAPS), and iterative decomposition of water and fat with echo asymmetry and least-squares estimation (IDEAL) were implemented and investigated.

Results—The different methods were compared with respect to the volume of positive contrast, the product of volume and signal intensity, imaging time, and the level of background suppression. Quantitative results are provided and strengths and weaknesses of the different approaches are discussed.

Conclusion—The appropriate choice of positive contrast imaging technique depends on the desired level of background suppression, acquisition speed, and robustness against artifacts, for which in vitro comparative data is now available.

Keywords

susceptibility imaging; off resonance; positive contrast

Introduction

Susceptibility changes often lead to unwanted artifacts in MR imaging. Recently there have been a growing number of applications that take advantage of local susceptibility differences (1). For example, in molecular imaging, stem cells are labeled with superparamagnetic nanoparticles (2,3) to enhance MR visibility, or iron uptake of macrophages supports

*Correspondence to: E.P.A. Vonken, UMC Utrecht, Dept Radiology, E01.132, Heidelberglaan 100, 3584CX Utrecht, evertjan@isi.uu.nl, Tel: +31-88-7556687, Fax: +31-30-2581098 .

visualization of atherosclerosis (4). Traditionally, local magnetic field susceptibilities are visualized as a local signal loss secondary to a decrease in T2*, such as in susceptibility weighted imaging (5). However, since signal loss sources are ambiguous, positive contrast methods have been developed. In fact, several different methods have been described. To increase the understanding and support a proper choice for the design of experiments, a subdivision in several categories is useful. One category of these methods exploits the local magnetic field gradients. These gradients are additive to the MR-imaging gradients and cause the local signal to undergo a shift in k-space (6). A second category exploits the change in the local Larmor frequency, i.e. off-resonance imaging (7,8). By selecting only parts of the frequency spectrum for imaging, positive contrast can be obtained. A third category of methods is based on phase accumulation which is exploited during steady-state free-precession and multi-echo imaging (9-11).

In this manuscript the focus is on six different positive contrast methods *in vitro*. Since in future applications the spatial distribution of the susceptibility markers will be important, only 3D implementations are investigated. Furthermore, to support future *in vivo* applications, cardiac triggering is incorporated as well as the presence of local saturation slabs.

The investigated methods include FLAPS (9), IRON (12), WM (13), SGM (14), IDEAL (15) and a frequency selective excitation (FSX) method. Quantitative parameters that were investigated to evaluate the performance of these techniques are the volume of enhancement, the amount of positive contrast (PC), the contrast-efficiency (CE) and the background-signal to noise ratio (BNR). A qualitative rating of the sensitivity of each method to global magnetic field inhomogeneities and RF inhomogeneities is provided as well.

Theory

The sensitivity of MR imaging to local magnetic field changes can be used to generate contrast. For a better understanding, it is useful to categorize the different positive contrast methods. For each of the following three categories two representative methods are evaluated and discussed. See also Table 1.

Local magnetic field gradients

A single spherical particle with radius a , placed in an external magnetic field B_0 , will induce a dipolar magnetic field disturbance described by

$$\Delta\mathbf{B}(r, \theta) = \Delta\chi a^3 (3\cos^2\theta - 1) B_0 / (3r^3), \quad [1]$$

with $\Delta\mathbf{B}(r, \theta)$ being the change in magnetic field including the Lorentz correction at distance $r > a$, θ the angle with respect to the main magnetic field, a the radius of the sphere, and $\Delta\chi$ the susceptibility difference to the background (16, p 569). The locally induced magnetic field gradient G_{susc} outside of the sphere can be written as $\mathbf{G}_{\text{susc}} = (\Delta\mathbf{B}/x, \Delta\mathbf{B}/y, \Delta\mathbf{B}/z)$ and will influence the MR signal formation of the material surrounding the sphere.

In general, the location of the MR signal in k-space is defined by

$$\mathbf{k}(t) = \gamma \int_0^t (\mathbf{G}_{\text{imaging}}(t') + \mathbf{G}_{\text{susc}}) dt' \quad [2]$$

where $G_{\text{imaging}}(t')$ are the time-dependent imaging gradients, t is the time of acquisition, and $\gamma \equiv \gamma/2\pi$, with γ the gyro-magnetic ratio for protons. Eq. 2 shows that the presence of the susceptibility gradients leads to a relative shift of the location of the MR signal in k-space by

approximately $\Delta k = TE \cdot G_{\text{susc}}$, since these gradients ‘act’ from excitation ($t=0$) to the echo-time ($t=TE$) (16, p 741).

WM—It is this shift in k -space that is exploited in the ‘white marker phenomenon’ (WM) method (13), also known as gradient echo acquisition for super-paramagnetic particles with positive contrast (GRASP) (17). Here, we will briefly explain the method along the lines of (6). It is graphically illustrated in Fig 1. By altering the imaging gradients (typically by reducing the strength of the slice select gradient) the portion of k -space that falls within the sampling window is shifted. Simultaneously, the background signal, that is unaffected by the susceptibilities, shifts out of this window. Typically, a shift of k_{max} is needed to make the background signal disappear. The signal from protons in close proximity to the susceptibility marker is shifted by Δk in k -space and when the relative shift of the imaging window (Δk_{WM}) is chosen appropriately, this signal will exclusively be visible, thus yielding positive contrast.

SGM—A second method that depicts local susceptibility gradients with positive signal is the Susceptibility Gradient Mapping (SGM) method (14,18). This method relies on post-processing alone and was implemented as an image filter: The region of size n pixels around every voxel is Fourier transformed into k -space. If there is no local magnetic field gradient, the spectrum is symmetrical. However, if local gradients are present, there will be a shift Δk of the peak of the spectrum in k -space. By calculating the magnitude of this shift in the three spatial directions and by calculating the absolute length of the ‘shift-vector’, a gradient magnitude map can be generated.

Local resonance frequency changes

As the local magnetic field in the surroundings of the susceptibility marker changes, the resonance frequency is shifted by Δf :

$$\Delta f = \gamma \Delta B. \quad [3]$$

This change can be exploited for positive contrast generation by altering an MRI sequence to either suppress the on resonant magnetization through magnetization preparation, or by using a frequency selective excitation in the imaging sequence.

IRON—An example for the above includes Inversion Recovery with ON-resonant water suppression (IRON) (12). The magnetization preparation using a prepulse is illustrated in Fig 2. An on-resonant ($\omega_{\text{IRON}}=0$ Hz) narrow bandwidth ($\Delta\omega_{\text{IRON}}$ typically 120 Hz) prepulse saturates the on-resonant background water signal, leaving only off resonant spins as signal sources in the image. Because fat is also off-resonant ($\omega_{\text{fat}} = -420$ Hz at 3T), an additional fat saturation pre-pulse can be added as needed. This prepulse is then followed by the imaging part of the sequence.

FSX—Frequency selective excitation (FSX) methods use an off resonance excitation pulse in the imaging part of the sequence. In order to combine this with 3D imaging and thus slice selection, a multiple wide-band excitation composite pulse can be used, such as a binomial pulse. In our implementation a fourth order (14641) scheme was used (8). The relative frequency response $S(f)$ of such a combination is

$$S(f) = \cos^4(\pi f \Delta t), \quad [4]$$

where $\Delta t = 1.16$ ms is the temporal spacing between the sub-pulses (19).

Local inter-echo phase changes

Strongly related to the category above are the positive contrast methods that exploit the phase that accumulates between two echoes. Two examples of such methods include steady-state with free precession and multi-echo acquisitions, respectively.

FLAPS—Fast Low Angle Positive contrast Steady-state free precession (FLAPS) exploits the phase rotation angle β between consecutive (phase cycled) RF excitations (9,10). On resonance, β is zero, but in the presence of a susceptibility marker,

$$\beta = \gamma TR \Delta B, \quad [5]$$

with TR being the repetition time of the imaging sequence. Since ΔB is spatially varying as described in Eq 1, there will be a signal (S) change around the marker, which is also dependent on the flip angle α and the T1/T2 ratio. In (9), the contrast $C(\beta)$, $C(\beta) = S(\beta) - S(0)$ as a measure of positive contrast, is described as

$$C(\beta) = S_0 \cdot \left(\frac{\sqrt{(2+2B) / (2(T1/T2)(1-A) + B(1+A) + A+1)} - 1 / ((T1/T2)(1-A) + A+1)} \right). \quad [6]$$

Here $S_0 = M_0 \cdot \sin(\alpha)$, M_0 is the equilibrium magnetization, $A \equiv \cos(\alpha)$ and $B \equiv \cos(\beta)$. For $C(\beta)$ to be positive, the flip angle is limited to $0 < \alpha < \arccos((T1/T2-1)/(T1/T2+1))$. In Fig 3, $C(\beta)$ is shown for several flip angles. For very small flip angles there is little signal and little positive contrast except in a small range of values for β . For intermediate flip angles, a large range for β yields positive contrast, albeit at the cost of the magnitude of contrast. For large flip-angles, the on resonant stimulated echoes dominate and at 90° , there is no positive contrast at all (negative contrast not shown in Fig 3). For a thorough discussion, see (9).

IDEAL—The second type of sequences exploiting the inter-echo phase differences are the multi gradient-echo methods combined with post-processing, sometimes referred to as Dixon methods (11,20). Although originally designed to separate water and fat signals, they are also well suited to visualize magnetic susceptibility markers (21). One implementation is Iterative Decomposition of water and fat with Echo Asymmetry and Least-squares estimation (IDEAL), as previously described (15). This method assumes the signal S to be composed by two distinct partitions that have a frequency difference Δf . The sum signal S_i for the i-th echo time TE_i is then described by

$$S_i = (W + F \cdot \exp(2\pi i \Delta f TE_i)) \cdot \exp(2\pi i \psi / TE_i), \quad [7]$$

with the signal W referring to the on resonance and F to the off resonance partition, respectively, and ψ is the complex field map, with $\text{RE}\{\psi\}$ the field offset (in Hz) and $\text{Im}\{\psi\} = 1/(2\pi T2^*)$ (15). The iterative algorithm will then estimate W, F and ψ from three echoes. The off resonance map of F then yields a positive contrast image.

Methods

Experimental setup

Following an earlier described experimental design (22), a single austenitic stainless steel sphere (FE 246805, diameter 0.5 mm AISI 316 steel, Goodfellow, Oakdale, PA) was submerged in 500 ml of gelatin (Jell-O, Kraft Foods, Rye Brook, NY) made from tap water doped with Gd-DTPA (1 mM, Magnevist, Berlex, Montville, NJ). The gelatin was cast in a plastic food container and a 50 ml layer of oil was placed on top to provide an additional source of off-resonant signal.

The phantom was positioned in an 8-channel Sense head-coil for signal reception and all imaging was performed on a clinical 3T MRI scanner (Achieva, Philips Healthcare, Cleveland, OH).

The imaging protocols for the different methods were defined as follows. First, all scans were performed using 3D segmented k-space data acquisition using artificial ECG triggering. This approach was chosen with future cardiovascular applications in mind. For each method, a 100ms acquisition window was used during every RR-interval (lasting 857ms). The total scan time was adjusted to allow for the acquisition of one complete k-space signal average for each method. The acquisition matrix in the coronal plane was $120 \times 120 \times 30$ with a field of view of $120 \times 120 \times 30 \text{ mm}^3$, and a reconstructed matrix of $240 \times 240 \times 60$. In axial scans, the rectangular field-of-view was changed to 80mm in anterior-posterior direction. The readout direction was concomitantly changed from foot-head to right-left. The receiver bandwidth was 217Hz/pixel. A saturation slab was applied in the sagittal direction to generate a local signal intensity variation independent of the susceptibility marker. Shimming and f_0 determination were performed using a previously described shimtool (23). The region of interest for shimming included most of the container. From all datasets modulus, real and imaginary DICOM images were stored for subsequent off-line analysis.

Data analysis

In the modulus images the center of the susceptibility marker was visually identified. Around this center, a shell with an inner radius of 21 voxels (where the expected maximum frequency change due to the marker was less than 5 Hz) and a thickness of 5 voxels was defined. In this shell that included 38641 voxels, the mean and standard deviation of the signal intensity were determined. The mean value divided by the standard deviation is a measure of the background signal of the phantom. This ratio will be referred to as background to noise ratio (BNR) in the following. Of the voxel-values inside the sphere enclosed by the shell, a cumulative histogram was created and a threshold was determined such that a fraction of 0.13% of the points exceeded this value. (In case of a normal distribution this would be 3 standard deviations above the mean). The threshold was applied to the sphere enclosed by the shell and the number of voxels (i.e. the enhanced volume) and the mean signal intensity were computed. Using the thus obtained values, positive contrast (PC) was calculated as the number of voxels times their signal intensity divided by the standard deviation of the shell (i.e. background variability). This number was divided by the square root of the scan time in seconds to obtain a measure of contrast efficiency (CE) (10). To minimize the influence of the choice of the center voxel, the above analysis was always repeated for its 26 neighboring voxels, and the results were averaged.

Phantom characterization

To estimate the off resonance frequencies and gradients present around the sphere, a short echo-time (1.4ms) phase-map was fitted using exhaustive parameter search to Eqs 1 and 3, where the phase relative to the background is $\varphi = \gamma \Delta \chi B_0 T E a^3 (3 \cos^2 \theta - 1) / 3r^3$. From the known radius a of the sphere, the susceptibility difference $\Delta \chi$ is thus obtained. From the multi-echo method described earlier, a $R2^*$ map was generated to estimate the $T2^*$ in the background. The $T2$ was obtained from a multi-spin echo sequence and $T1$ was estimated using a Look-Locker sequence, both available on the scanner (16, p 650).

Positive contrast imaging

WM—Image acquisitions were performed with shortest TR (ranging from 6.8ms to 12.7ms, depending on the required size of the dephasing gradient). For each TR, the shortest possible

echo time was used. The pulse train length was adjusted to fit to the 100ms window (ranging from 8 to 14 excitations), the RF excitation angle was 10° .

The following dephasing gradients expressed in units of k_{\max} of the reconstructed image were chosen in the slice select direction: $0, \pm 0.4, \pm 0.6 \pm 0.8, \pm 1.0, \pm 1.4, \pm 2.0, \pm 4.0, \pm 6.0 k_{\max}$. Imaging was performed in the coronal and axial plane, with the readout direction in parallel and perpendicular to B_0 , respectively. In the coronal orientation, additional experiments were performed with dephasing in the phase and frequency encoding direction, with dephasing strengths up to $\pm 1.4 k_{\max}$.

SGM—The post-processing method was applied to images with TR/TE=6.8/3.2ms, pulse train length 14, RF excitation angle 10° . The filter kernel-sizes were 3, 5 and 7 pixels, equal in the spatial directions. Images in both coronal and axial orientation were processed.

IRON—The settings of the prepulse were optimized for every $\Delta\omega_{\text{IRON}}$ investigated using 2D scout scans that loop over a range of flip angles of the prepulse ($\alpha_{\text{IRON}}=80^\circ$ to 140° in increments of 5°) with a fixed $\omega_{\text{IRON}}=-25$ Hz. Subsequently the center frequency of the suppression pulse was varied from -300 Hz to 300 Hz in steps of 25 Hz using a $\Delta\omega_{\text{IRON}}=102$ Hz. The suppression angle and center-frequency that led to the best background suppression were visually identified. Subsequently, 3D images were acquired in coronal and axial orientation with prepulse bandwidths of 102, 196 and 392Hz, respectively. Parameter optimization and image acquisition were performed for both fast spin echo and gradient echo acquisitions. Imaging parameters for the gradient echo images were TR/TE=6.8/3.3ms, RF excitation angle 10° , pulse train length 14. For the fast spin echo imaging sequence TR=857ms, TE=11ms, 90° excitation angle, 180° refocusing angle, echo train length 9, bandwidth 282Hz/pixel.

FSX—TR/TE=11.3/5.5ms, RF excitation angle 13° , pulse train length 8. A 14641-binomial pulse consisting of 5 sinc-gaussian (5 periods) sub-pulses was used for excitation. Using the interface of the shimtool, an offset of $0, \pm 100, \pm 200, \pm 300$ and ± 420 Hz was added to the on resonance excitation frequency f_0 . Images in a coronal and axial plane were acquired.

FLAPS—In order to minimize TR, the bandwidth of the acquisition was increased relative to the other imaging techniques to 1320Hz/pixel. Other scan parameters were ranging from TR/TE=2.8/1.4ms with a pulse train length of 35 for a 1° RF excitation angle, to TR/TE=3.7/1.9ms for an RF excitation angle of 50° (pulse train length of 26). Images were acquired in a coronal and axial orientation.

IDEAL—The IDEAL method was applied to MRI image data sets that were obtained with three different echo times. The first set of three with an inter-echo spacing of 1.0 ms (these images were acquired as separate scans with a single TE). Here TR/TE₁=9.0/3.3ms, RF excitation angle 10° , pulse train length 11. The second and third sets were acquired as multi-echo acquisitions (with fly-back to have the readout in the same direction for each echo). The second set had an echo spacing of 2.3ms achieved by increasing the bandwidth from 217 to 1320Hz/pixel resulting in TR/TE₁=8.0/1.5ms, RF excitation angle 11° , pulse train length 12. The third set had an echo spacing of 5.8ms, with TR/TE₁=19/3.2ms, RF excitation angle 17° , pulse train length 5. Images in a coronal and axial orientation were acquired for set 1, sets 2 and 3 in an axial plane.

Results

Phantom characterization

The fitted frequencies from the phase map of the surroundings of the marker are shown in a coronal cross-section in Fig 4. The matching susceptibility (difference) of the sphere was $\Delta\chi=4.3\cdot 10^{-3}$. As the area of phase wraps (distance ~ 4 pixels to the center) was excluded from the fit, the local minimum was very sharply defined (<1% variability in fitted parameters). The ‘magnetic strength’ $4\pi a^3/3\cdot\Delta\chi$ is thus well determined, the size of the sphere however, is only known within 5%, thus the accuracy is estimated to be around 15% (i.e. $\Delta\chi=4.3\cdot 10^{-3}\pm 0.6\cdot 10^{-3}$). The measured T1 in the background of the doped gelatin was 92 ± 3 ms, T2 was 49 ± 2 ms and T2* was 48 ± 5 ms.

Positive contrast imaging

WM—As a function of the strength of the dephasing gradient, the volume of positive contrast, PC, CE and BNR are shown in Fig 5a-d. For zero dephasing, a regular segmented gradient echo image is obtained that already shows some positive contrast. This is caused both by statistical noise and by signal enhancement as a result of image distortion (see Discussion). With small dephasing there is an increase in the amount of positive contrast, as shown in Fig 5b. However, as can be derived from Fig 5d, the background is not well suppressed. For dephasing of $0.6\cdot k_{\max}$ and higher, there is a transition, after which the background suppression is very effective. However, in regions where the signal intensity is rapidly changing in the dephasing direction, background signal suppression is challenging (see Fig 6a-c). The maximum amount of contrast is obtained when imaging is performed in the axial plane. The coronal plane dephasing shows generally less positive contrast enhancement, illustrating the directional sensitivity of this method.

SGM—The positive contrast as measured using the SGM method is shown in Fig 5e-h. The PC and volume of enhancement do not show a significant dependence on the analysis kernel size and are higher than the values obtained with WM (Note the larger scale on the y-axis in Fig 5f.). Since the method relies on post-processing, the scan time efficiencies are equal for different kernel sizes (post processing time is not included).

IRON—The results for the IRON method are shown in Fig 5i-l. Lower prepulse bandwidths result in more contrast. The amount of positive contrast with FSE and TFE is similar. Image orientation does not affect the contrast generation. Despite the scantime being twice as long for FSE as compared to TFE, the scan time efficiency is still similar. In all cases, good background suppression was achieved (BNR <5, see Fig 5-l).

FSX—The measured contrast as a function of the detuning of the binomial RF pulse frequency is shown in Fig 5m-p. As the method selectively enhances either positive or negative frequencies, the enhancement has a different distribution in space, but the amount of enhancement is similar for negative and positive frequencies (see Fig 5n). The spatial orientation of the image plane affects the efficiency, which is somewhat better in the axial plane, shown in Fig 5-o. The BNR shown in Fig 5-p suggests that only for large off resonances adequate suppression is achieved, coinciding with a minimum magnitude of PC.

FLAPS—The results for the FLAPS method are shown in Fig 5q-t. For small RF excitation angles, there is an increase in positive contrast volume and magnitude as a function of the RF excitation angle. However, for excitation angles of 5° and larger, a constant but rather small PC is measured. PC does not depend on the image orientation. As the increase in TR for these relatively small flip-angles is small, CE shows a plateau as well. Since these sequences are fast, albeit with a lower total amount of PC, the CE is comparable to WM,

IRON, and FSX. In this respect, the faster axial image orientation (smaller matrix) outperforms the scan obtained in the coronal orientation. The BNR is monotonously increasing as a function of the flip-angle. A BNR > 5 is already occurring at a flip-angle of 2°, making the background suppression poor for larger flip-angles.

IDEAL—The positive contrast measurements on the IDEAL reconstructed off resonance images are shown in Fig 5u-x. The slice orientation does not affect PC. The PC is very high (different vertical scale) as is the CE. However, the images acquired with the larger bandwidth (sensitive to 145 Hz off resonance) show significantly less positive contrast. Although the scan time is shorter, the CE is lower in this case as well. Fig 5-x shows excellent background suppression for the IDEAL method.

In Fig 6, a composition is made from typical example images of the different methods.

Discussion

In this paper, the amount of positive contrast that is produced *in vitro* by six different positive contrast techniques was compared. The positive contrast was quantified both as the enhanced volume and as a normalized measure incorporating the volume and the strength of enhancement expressed as the contrast-to-noise ratio (analogous to (9)). The normalization of the contrast allows for a direct comparison between the different methods, all having acquired one full k-space.

The setup of this study was aimed at imaging a comprehensive phantom containing a single metal sphere as susceptibility marker. This simplifies analysis, as the distribution of multiple susceptibility sources increases the complexity considerably. When many markers are in close proximity, they will behave as a bulk susceptibility as opposed to individual dipoles (16, p 762). Furthermore, we have chosen to limit this study to 3D Fourier based acquisition methods only. Although excellent positive contrast results have been published for 2D or projection imaging (7), the ability to perform 3D rather than 2D or projection imaging will be important for accurate localization and potentially for the quantification of such susceptibility markers. The value of recent non-Fourier based methods, e.g. ultra short echo time radial sampling (24), is also beyond the scope of this comparison.

In preparation of future *in-vivo* applications, all sequences were implemented for triggered segmented imaging protocols (10). However, some of the methods could easily be combined with a steady state sequence, thus leading to a significant abbreviation in scanning time as shown in Table 2. A distinct advantage of the segmented scans, however, is that there is time within the sequence for the magnetization preparation irrespective of the choice of imaging parameters. A third choice in the present study was a fixed acquisition window of 100ms only, which leads to different scan times as the repetition time differs among the six methods. The relative time advantage of a certain method can thus be deduced from the contrast efficiency measure.

A distinct limitation of our comparison study, is that only WM and IRON were developed in our own institutions. The other methods were implemented from information in the literature. Although effort was put into optimizing each of these methods, individual methods might have had better implementations in other centers. This universal shortcoming is not easily addressed and probably would require a universal phantom to be imaged at different sites according to prescribed requirements. This would make the head-to-head comparison between methods fairer, at the price of introducing scanner hardware variability (compare e.g. www.grand-challenge.org for image processing algorithms).

WM—A consistent finding for this method is that positive contrast is observed even without dephasing. The local susceptibility gradients added to the read-out gradient result in image distortion with signal accumulation and thus bright spots that are above the noise determined threshold for positive contrast. This effect is strongly related to the strength of the read-out gradient relative to the local susceptibility gradients (25). Note that this signal distortion is present in all the positive contrast methods (including FSE based acquisitions), but it is particularly apparent in small bandwidth 3D-WM.

The PC shown in Fig 5 has a maximum which is comparable to that of IRON and which is lower than that of IDEAL and SGM, and higher than that of FLAPS and FSX. The optimal enhancement is, however, sensitive to the choice of the dephasing strength. As the dephasing is expressed relative to k_{\max} this means that with a given susceptibility gradient, the WM contrast depends on the resolution (i.e. slice thickness for through plane dephasing) of the imaging sequence. In general, however, the susceptibility induced k-space shifts are less than k_{\max} and the positive contrast is optimal when the background is shifted out of the k-space imaging window. As k_{\max} is known beforehand from the imaging resolution, this sensitivity to the magnitude of the dephasing does not pose a problem in practice. The background suppression after the transition is adequate and comparable to that of IRON, SGM and IDEAL.

Other positive contrast comparison studies have been published using a decreased refocusing gradient in combination with 2D imaging (21,26). The dephasing prescribed in this manner will depend on the bandwidth of the excitation pulse. However, and since these sequence details are not provided in these reports, the magnitude of both dephasing and positive signal response remains unclear and cannot currently be compared to the findings from our study. For future and direct comparisons, we therefore propose to use units of k_{\max} , which, for a 2D slice, would be $1/(2 \cdot \text{slice thickness})$.

In the literature, it has been described that the contrast of WM is less stable at 3T than at 1.5T (17). It is our experience, that the positive contrast is very robust at 3T, but that a proper Larmor frequency determination (f_0) is imperative (see Table 2). An offset frequency will shift the k-space imaging window, and while for regular imaging this typically goes unnoticed, for WM imaging, this will offset the contrast curve, which may influence the amount of contrast obtained in the image. As an offline B_0 -map based shimming tool with integrated f_0 determination was used, this effect was minimized in our experiments.

A feature that is prominent in WM is the sensitivity to signal intensity changes in the dephasing direction. High frequency signal intensity changes, which for partial volume effects have frequency components outside the imaging window, will lead to a positive response and therefore concomitant unwanted positive contrast. In Fig 6A-c, this is confirmed by the enhancement seen at the edges of the saturation slab, where no susceptibility changes were present. At the borders of the phantom a combined (stronger) enhancement is seen, possibly by a combination of susceptibility changes (in the left-right direction) at the edge of the phantom and partial volume effects. Methods have been devised to circumvent this property of the WM method based on multiple acquisitions with different dephasing, at the cost of overall scanning time (27).

SGM—The positive contrast that this method extracts from the images is very high, only equaled by the other post-processing method IDEAL. In combination with good background suppression, this method shows great promise for *in vivo* applications. In a comparison study with labeled cells, Liu et al. showed superior contrast as compared to WM and IRON (2). While we also find higher contrast than with IRON and WM, our results seem to differ only by a factor of about two, particularly for IRON with a small bandwidth pre-pulse.

Possible explanations include that in their study, a 3D SGM technique was compared to 2D WM and IRON implementations. Moreover, the amount of dephasing for the WM method is difficult to compare among different studies and the pre-pulse for IRON was different (high bandwidth with a wide Gaussian frequency distribution). Furthermore, as in the present study, second order shimming could have supported the use of a smaller bandwidth of the IRON pre-pulse.

In SGM the echo time determines the size of the volume of positive enhancement. While we investigated only one echo time, Eq 2 shows a linear relation with ΔG . When a certain application requires more sensitivity (but not necessarily more CNR as the noise will increase and a $T2^*$ dependent signal loss will occur), the echo time could be increased. However, the importance of this effect remains to be determined in practice.

As SGM operates in all spatial directions, there is no inherent directional sensitivity as found for WM. However, when the signal is not completely real, a signal intensity change in the modulus image (e.g. through partial volume effects) may be asymmetrical in k-space. This will generate some positive contrast at these interfaces. Because large phase gradients in the background are corrected by shimming, the effect is less prominent than for WM. Compare for example Fig 6B-d with Fig 6A-c, where the signal intensities at the edge of the saturation band are less in the SGM image.

IRON—While the previous methods were based on local gradients, IRON is based on the local field strengths. The induced resonance frequency offsets are exploited by tailoring the pre-pulse to select only on resonant water. However, this also highlights the main concerns associated with this method: the center frequency has to be determined accurately, the background field has to be as homogeneous as possible (through shimming), and the RF excitation angle has to be well determined spatially, which, at high field strengths may be challenging due to B_1 inhomogeneity. In Fig 6C-b the border of the phantom is not completely suppressed, as with the smaller bandwidth in Fig 6C-a: the shimming was the same and thus the effect can be attributed to RF inhomogeneity. The signal at the top and bottom of Fig 6C-c (and to a lesser extent in Fig 6C-a) is likely residual B_0 inhomogeneity (as it is directed in parallel to the main magnetic field). However, with the use of our shimming method, the effects are well controlled and the amount of positive contrast is comparable to WM, less than IDEAL and SGM and better than FLAPS and FSX. The background suppression is good and comparable to WM, IDEAL and SGM. However, as for all methods except for WM and SGM, there is an off resonant signal from fat, see Fig 6C-d (arrow). As this may be a drawback *in vivo*, this will require an additional fat-suppression pre-pulse. The effectiveness of the rest-slab in the images, shows that IRON and all other methods are compatible with pre-pulses, and that in practice, this should not pose a problem. An advantage of IRON being based on the use of a pre-pulse, is that the readout of the sequence is not affected, which allows greater flexibility than WM, FLAPS, FSX and the sequences for IDEAL and SGM. For example (fast) spin echo as well as gradient echo can be used with similar results. Other possibilities include fractional echo imaging and non-Cartesian acquisitions.

FSX—As the originally described version of this method (28) uses projection images, directly extending it to 3D imaging is not trivial and would be beyond the scope of this comparison. Therefore, to illustrate the concept we used a spectral-spatial binomial pulse for off-resonance excitation (8). Both a feature and a limitation is that FSX selectively visualizes either positive or negative frequency shifts (compare Fig 6E-b and Fig 6E-c). However, as the frequency response of the spectral-spatial pulse is periodical, care has to be taken in interpreting images if very large frequency shift are expected. The FSX method is sensitive to B_0 inhomogeneities, as these will inevitably lead to enhancement as well. The

adverse effects of RF inhomogeneity will likely be less than for magnetization preparation (IRON), as the amount of signal will change, but the relative strength of the subpulses remains constant. Another disadvantage of these pulses is that the frequency response for lower order pulses is not that sharp and echo time increases rapidly with higher order pulses (see Fig 3). While the periodicity is not a big problem, the gradual slope makes for mediocre background suppression, unless close to the actual maximum off resonance (in our case at ± 420 Hz). As the off resonance induced by the susceptibility marker is already diminishing for these large offset frequencies, the amount of positive contrast in combination with good background suppression is less than for WM, SGM, IDEAL and IRON. The background suppression is comparable to FLAPS, which also shows a narrow optimum. The curve for BNR shows a peak not exactly centered around zero, but is biased towards negative frequencies. This occurs for both phantom orientations and may be due to small pulse errors, e.g. due to Eddy currents or timing offsets in the sequence (19). The use of even number binomial sign changing pulses (e.g. 1331) might help in this respect, but the amount of positive contrast is probably not affected significantly, as there is only a slight asymmetry visible in the two local maxima around zero for PC. Also, the RF refocusing properties of these composite pulses is not optimal for short $T2^*$ situations. In general, a better performance exploiting frequency selective excitation is expected with special excitation pulses, designed for sharp spectral transitions, short durations and self refocusing allowing for short echo times. While these pulses have been applied using projection imaging, more recently 3D-capable implementations have been presented, but these designs are far from trivial and were not available during the time of the experiments (29).

FLAPS—The FLAPS method exploits the properties of balanced SSFP imaging, and is thus a very fast method without the need for post-processing or special pre-pulses. With the small flip-angles involved, power deposition limitations will not be an issue even at higher magnetic field strength, as it may be with e.g. IRON-FSE. The amount of positive contrast is reduced when compared to the other techniques except FSX, but the contrast efficiency is comparable to WM and IRON. However, the potential drawback is that the background suppression is not as good as for WM, SGM, IRON and IDEAL. The background signal is directly related to the applied flip angle and except when it is very small ($\sim 1^\circ$), the BNR is large. A second disadvantage is that FLAPS is susceptible to suboptimal shimming, giving rise to dark band like artifacts, see Fig 6D-d. Improvements of the method can be achieved by combining it with background suppression techniques (such as WM and IRON (30)), but this was beyond the scope of this comparison.

IDEAL—While FSX exploits phase evolution during excitation, IDEAL uses phase accumulation between echoes. This method is a descendent of the earlier reported phase imaging methods (31,32). Having three complex images allows for determination of two frequency components together with the field map, containing both phase and $T2^*$ information (15). More echoes allow for the extraction of more components, but this lengthens the acquisition time. A disadvantage of this method is the need for (closely separated) multiple echoes. If the spacing is too short, multiple acquisitions will have to be acquired. However, IDEAL appears to better suppress the background than FSX, which signifies a difference in the frequency separation obtained by FSX and IDEAL in our implementation. The frequency separation is influenced by the phase accumulation between the echoes: if for a certain echo time increment a frequency difference is assumed that yields a phase unequal to $2\pi/3$, the frequency separation is negatively influenced (21). Note that as with FSX, the frequency response is cyclic and that aliasing may occur, if large echo spacings are used.

When measuring PC, the IDEAL performs similar as SGM, better than WM, IRON and FLAPS, and much better than FSX. The background suppression is good. The results are,

however, dependent on the SNR in the source images: when using a higher bandwidth (lower SNR), the positive contrast is reduced (see Fig 5-v).

The presented comparison study did not compare all the previously published methods for positive contrast imaging (e.g. (24,33,34)). Moreover, for the methods that were included in the comparison, neither every aspect nor variant have been investigated. The selection of the methods was based on which appeared to be the most commonly used in its class. Care was taken to maximally generate PC in the experiment for each technique. With respect to implementation details, the WM and IRON method have been developed in our labs, thus giving them an advantage over the other methods. While we do not expect that small details and experience will dramatically change the amount of PC, particularly robustness and *in vivo* applicability may be influenced greatly.

In the comparison presented above, it was beneficial for clarity to compare them in a simple phantom using a standardized imaging protocol. However, some aspects still remain to be investigated and include the influence of field strength, which is directly related to susceptibility and shimming sensitivity and SNR. Also, the influence of spatial resolution and background inhomogeneity, the influence of flow and motion, the number of magnetic disturbers and their (spatial) distribution and the proportionality of the positive contrast to the amount of markers or the marker material (35,36). Since these last properties are application (anatomy) dependent, implementation details will become important. This was, unfortunately, outside the scope of our present study.

Conclusion

It has been shown that for static 3D imaging, positive contrast from a susceptibility marker can be obtained using different methods. The magnitude of contrast is similar for the white marker method, for Inversion Recovery with ON-resonant water suppression, and slightly less for Fast Low Angle Positive contrast Steady-state free precession and for Frequency selective excitation. The post-processing methods Iterative Decomposition of water and fat with Echo Asymmetry and Least-squares estimation and susceptibility gradient mapping lead to a higher contrast. The temporal scan-efficiency was highest for IDEAL and SGM, followed by WM, IRON and FLAPS. FSX had the lowest efficiency. Background suppression was best for WM, SGM, IRON and IDEAL. Good suppression for FLAPS and FSX was only achieved in a very narrow parameter range.

Overall this comparison suggests that any of the investigated 3D positive contrast imaging techniques may be used for visualization of susceptibility markers. The appropriate choice will depend on the required level of background suppression, acquisition speed, B_0 and B_1 sensitivity, flexibility and availability on the MRI systems.

Acknowledgments

We would like to thank J-H Seppenwoolde for providing us with the susceptibility marker used to build the phantom.

This work is supported in part by the NIH/NHLBI grant HL084186. Dr. Stuber is compensated as a consultant by Philips Medical Systems NL, the manufacturer of equipment described in this presentation. The terms of this arrangement have been approved by the Johns Hopkins University in accordance with its conflict of interest policies.

References

1. Reichenbach JR, Venkatesan R, Yablonski DA, Thompson MR, Lai S, Haacke EM. Theory and application of static field inhomogeneity in gradient-echo imaging. *J Magn Reson Imaging*. 1997; 7:266–79. [PubMed: 9090577]
2. Liu W, Dahnke H, Jordan EK, Schaeffter T, Frank JA. In vivo MRI using positive-contrast techniques in detection of cells labeled with superparamagnetic iron oxide nanoparticles. *NMR Biomed*. 2008; 21:242–50. [PubMed: 17566968]
3. Kraitchman DL, Tatsumi M, Gilson WD, et al. Dynamic imaging of allogeneic mesenchymal stem cells trafficking to myocardial infarction. *Circulation*. 2005; 112:1451–61. [PubMed: 16129797]
4. Korosoglou G, Weiss RG, Kedziorek DA, Walczak P, et al. Noninvasive Detection of Macrophage-rich Atherosclerotic Plaque in Hyperlipidemic Rabbits using ‘Positive Contrast’ Magnetic Resonance Imaging. *J Amer Coll Cardiol*. 2008; 52:483–91. [PubMed: 18672170]
5. Chavhan GB, Babyn PS, Thomas B, Shroff MM, Haacke EM. Principles, techniques, and applications of T2*-based MR imaging and its special applications. *Radiographics*. 2009; 29:1433–49. [PubMed: 19755604]
6. Bakker CJ, Seppenwoolde J-H, Vincken KL. Dephased MRI. *Magn Reson Med*. 2006; 55:92–7. [PubMed: 16342154]
7. Edelman RR, Storey P, Dunkle E, et al. Gadolinium-Enhanced Off-Resonance Contrast Angiography. *Magn Reson Med*. 2007; 57:475–84. [PubMed: 17326177]
8. Patil, S.; Boller, C.; Bilecen, D.; Scheffler, K. Visualization of the Paramagnetic Markers in Interventional MRI Using Spatial-Spectral Pulses; Proceedings of the 15th Annual Meeting of ISMRM; Berlin, Germany. 2007; p. 1122
9. Dharmakumar R, Koktzoglou I, Li D. Generating positive contrast from off-resonant spins with steady-state free precession magnetic resonance imaging: theory and proof-of-principle experiments. *Phys Med Biol*. 2006; 51:4201–15. [PubMed: 16912377]
10. Dharmakumar R, Koktzoglou I, Li D. Factors influencing fast low angle positive contrast steady-state free precession (FLAPS) magnetic resonance. *Phys. Med. Biol*. 2007; 52:3261–73. [PubMed: 17505101]
11. Bernstein, MA.; King, KF.; Zhou, XJ. Handbook of MRI Pulse Sequences: A Guide for Scientists, Engineers, Radiologists, Technologists. Academic Press; 2004. p. 857-86.
12. Stuber M, Gilson WD, Schär M, et al. Positive contrast visualization of iron oxide-labeled stem cells using inversion-recovery with ON-resonant water suppression (IRON). *Magn Reson Med*. 2007; 58:1072–7. [PubMed: 17969120]
13. Seppenwoolde J-H, Viergever MA, Bakker CJ. Passive tracking exploiting local signal conservation: the white marker phenomenon. *Magn Reson Med*. 2003; 50:784–90. [PubMed: 14523965]
14. Dahnke H, Liu W, Herzka D, Frank JA, Schaeffter T. Susceptibility gradient mapping (SGM): a new postprocessing method for positive contrast generation applied to superparamagnetic iron oxide particle (SPIO)-labeled cells. *Magn Reson Med*. 2008; 60:595–603. [PubMed: 18727097]
15. Yu H, McKenzie CA, Shimakawa A, et al. Multiecho reconstruction for simultaneous water-fat decomposition and T2* estimation. *J Magn Reson Imaging*. 2007; 26:1153–61. [PubMed: 17896369]
16. Haacke, EM.; Brown, RW.; Venkatesan, R.; Thompson, MR. Magnetic Resonance Imaging: Physical Principles and Sequence Design. Wiley-Liss; 1999.
17. Mani V, Briley-Saebo KC, Itskovich VV, Samber DD, Fayad ZA. Gradient echo acquisition for superparamagnetic particles with positive contrast (GRASP): sequence characterization in membrane and glass superparamagnetic iron oxide phantoms at 1.5T and 3T. *Magn Reson Med*. 2006; 55:126–35. [PubMed: 16342148]
18. Vonken EJ, Schär M, Stuber M. Positive contrast visualization of nitinol devices using susceptibility gradient mapping. *Magn Reson Med*. 2008; 60:588–94. [PubMed: 18727096]
19. Hore PJ. A new method for water suppression in the proton NMR spectra of aqueous solutions. *J Magn Reson*. 1983; 54:539–42.

20. Reeder SB, Wen Z, Yu H, et al. Multicoil Dixon Chemical Species Separation with an Iterative Least-Squares Estimation Method. *Magn Reson Med*. 2004; 51:35–45. [PubMed: 14705043]
21. Reeder, SB.; Faranesh, AZ.; Chen, IY., et al. Off-Resonance Separation for Positive Contrast Imaging of Iron-Oxide Labeled Cells; Proceedings of the 14th Annual Meeting of ISMRM; Seattle, Washington, USA. 2006; p. 430
22. Seppenwoolde, J-H.; Oude Engberink, R.; van der Toorn, A.; Blezer, EL.; Bakker, CJ. Selective MRI of magnetically labeled cells - a comparative evaluation of positive contrast techniques; Proceedings of the 14th Annual Meeting of ISMRM; Seattle, Washington, USA. 2006; p. 360
23. Schär M, Kozerke S, Fischer SE, Boesiger P. Cardiac SSFP imaging at 3 Tesla. *Magn Reson Med*. 2004; 51:799–806. [PubMed: 15065254]
24. Seevinck PR, de Leeuw H, Bos C, Bakker CJ. Highly localized positive contrast of small paramagnetic objects using 3D center-out radial sampling with off-resonance reception. *Magn Reson Med*. 2011; 65:146–56. [PubMed: 20740656]
25. Posse S, Aue WP. Susceptibility Artifacts in spin-echo and gradient-echo imaging. *J Magn Reson*. 1990; 88:473–92.
26. Warmuth, C.; Schnorr, J.; Wagner, S. Iron oxide enhancing atherosclerotic plaque: Feasibility of white marker imaging techniques; Proceedings of the 15th Annual Meeting of ISMRM; Berlin, Germany. 2007; p. 436
27. Seppenwoolde J-H, Vincken K, Bakker CJ. White marker imaging - separating magnetic susceptibility effects from partial volume effects. *Magn Reson Med*. 2007; 58:605–9. [PubMed: 17628486]
28. Cunningham CH, Arai T, Yang PC, McConnell MV, Pauly JM, Conolly SM. Positive contrast magnetic resonance imaging of cells labeled with magnetic nanoparticles. *Magn Reson Med*. 2005; 53:999–1005. [PubMed: 15844142]
29. Balchandani P, Yamada M, Pauly J, Yang P, Spielman D. Self-refocused spatial-spectral pulse for positive contrast imaging of cells labeled with SPIO nanoparticles. *Magn Reson Med*. 2009; 62:183–92. [PubMed: 19449385]
30. Bieri, O.; Patil, S.; Scheffler, K. Morphing-SSFP: A new method for fast detection of strong magnetic field inhomogeneities and its application for tracking ferromagnetic devices; Proceedings of the 15th Annual Meeting of ISMRM; Berlin, Germany. 2007; p. 294
31. Dixon, WT.; Kulkarni, AM.; Meyer, DE.; Bales, BC.; Foo, TK. Quantification of SPIO iron: Comparison of three methods; Proceedings of the 15th Annual Meeting of ISMRM; Berlin, Germany. 2007; p. 1892
32. Kim, Y.; Bae, K.; Yoo, S-S.; Park, T.; Park, H. Positive Contrast MRI of Magnetically labeled Human Cervical Carcinoma Cells and Tumor Monitoring; Proceedings of the 15th Annual Meeting of ISMRM; Berlin, Germany. 2007; p. 1216
33. Overall, WR.; Pauly, JM. Field-encoded SSFP: A new method for positive-contrast visualization of paramagnetic agents; Proceedings of the 15th Annual Meeting of ISMRM; Berlin, Germany. 2007; p. 579
34. Coolen, BF.; Lee, P.; Shuter, B.; Golay, X. Optimized MRI parameters for positive contrast detection of iron-oxide labeled cells using double-echo Ultra-short echo time (d-UTE) sequences; Proceedings of the 15th Annual Meeting of ISMRM; Berlin, Germany. 2007; p. 1224
35. Varma G, Pedersen SF, Taupitz M, Botnar RM, Dahnke H, Keevil SF, Schaeffter T. Utilizing different methods for visualizing susceptibility from a single multi-gradient echo dataset. *MAGMA*. 2009; 22:297–308. [PubMed: 19644720]
36. Zhao Q, Langley J, Lee S, Liu W. Positive contrast technique for the detection and quantification of superparamagnetic iron oxide nanoparticles in MRI. *NMR Biomed*. 2011; 24:464–72. [PubMed: 20931569]

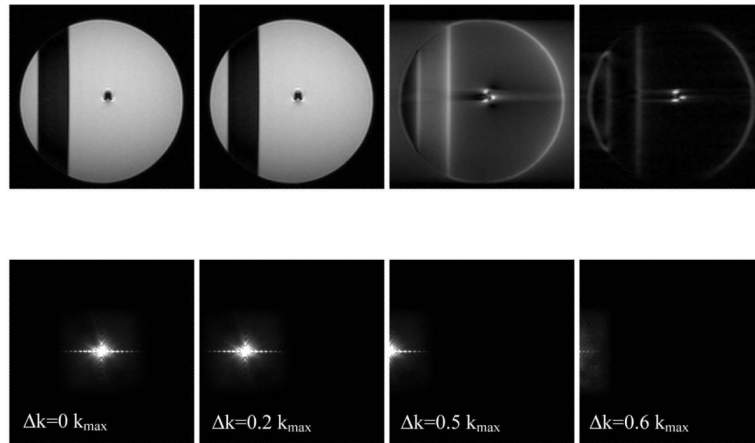


Fig 1. Demonstrating the effect of shifting the k-space in the left-right direction. Top row: modulus images, bottom row modulus of the k-space spectrum (The window level in the right column is 10 times smaller than in the first three). As long as the center peak ($k=0$) falls in the reconstruction window, the background is preserved. After a shift of approximately $0.5 \cdot k_{\max}$ the positive contrast appears.

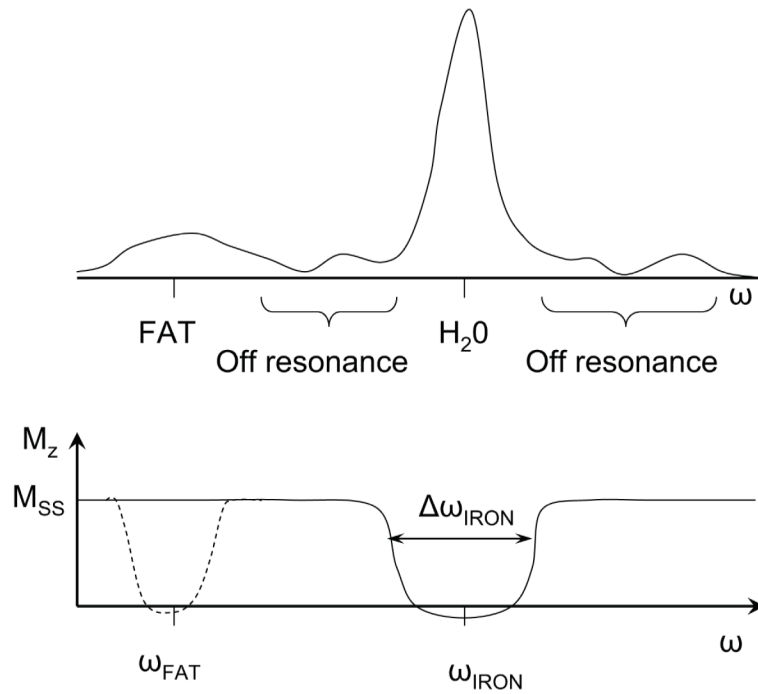


Fig 2.

Schematic drawing of the spectrum (top graph) with the on resonant water peak and the (off resonant) fat peak (separated by 420 Hz at 3T). The susceptibility marker will induce off-resonant signal outside of the water-peak (marked 'off resonance'). By a frequency selective IRON-prepulse (centered at $\omega_{IRON}=0$ Hz and with bandwidth $\Delta\omega_{IRON}$) the on resonant signal is suppressed relative to the off resonant magnetization, which remains as steady-state magnetization (M_{SS}) immediately before imaging (bottom graph). An optionally added fat saturation can additionally suppress frequencies around the fat peak (dashed line).

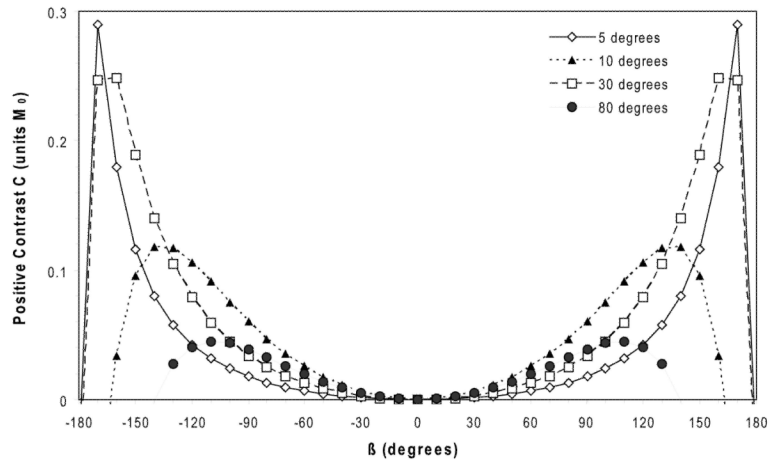


Fig 3. Positive contrast signal C in units of the equilibrium magnetization M_0 using the Fast Low Angle positive contrast Steady-state precession for $T_1/T_2=2$ as a function of the phase rotation angle between two excitations. On resonance ($\beta=0$) there is no signal, while for a certain range of β -values the off resonant signal is larger than on resonant, yielding the positive difference (i.e. contrast).

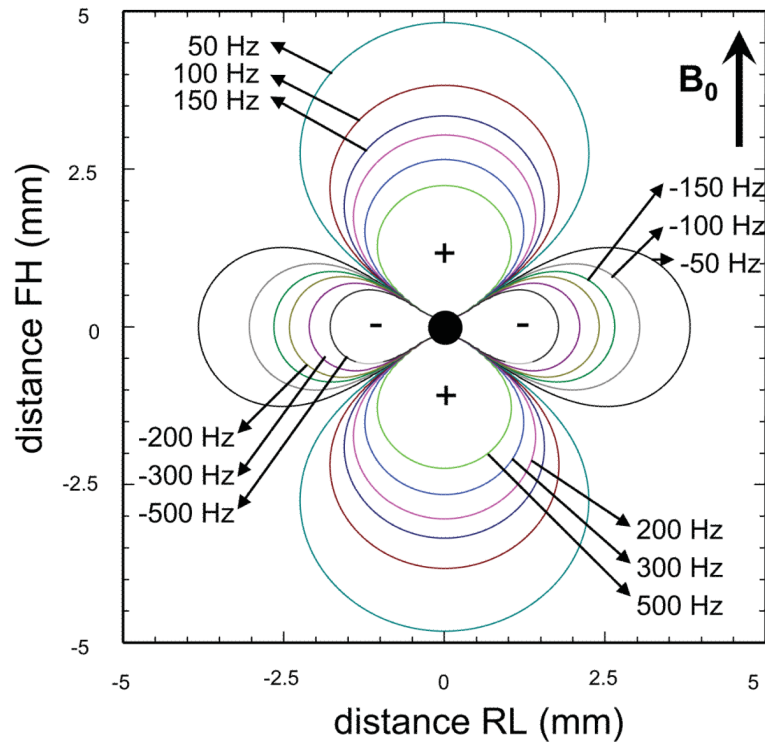


Fig 4. Schematic of the iso-frequency shift lines as defined in Eqs 1 and 3 around the susceptibility marker in the coronal plane: the vertical axis is parallel to B_0 and the horizontal axis is perpendicular to B_0 . Shown are the frequency shifts of 50, 100, 150, 200, 300 and 500 Hz. Notice that closer to the marker, the isolines are grouped closer together giving rise to intra-voxel phase dispersion. The diameter of the sphere was 0.5mm. Fitting the frequency distribution to a measured phase map with $TE=1.4$ ms, the susceptibility is found to be $\Delta\chi=4.3\cdot 10^{-3}$.

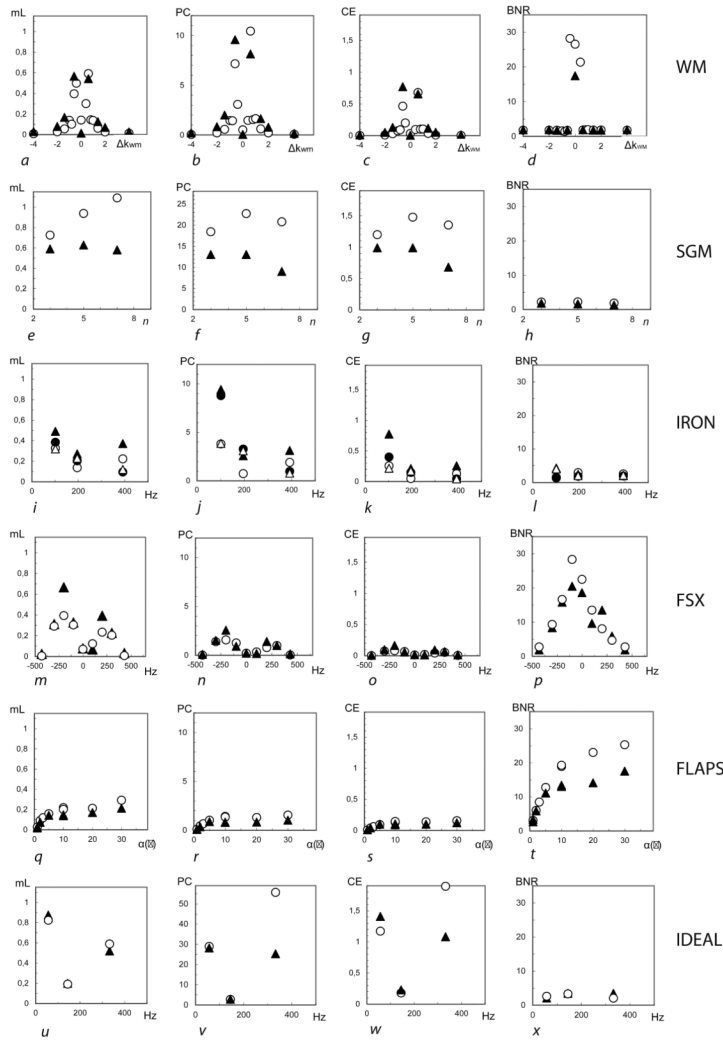


Fig 5. Measures of positive contrast for the different methods. For white marker (WM) the (a) enhanced volume (in mL), (b) positive contrast (PC), (c) contrast efficiency (CE) and (d) background to noise level (BNR) are shown for the coronal (○) and transverse (▲) plane as a function of the dephasing strength (Δk_{WM} expressed in units of k_{max}). At 0 dephasing, a regular gradient echo image is analyzed. For susceptibility gradient mapping (SGM) the (f) enhanced volume, (g) PC, (h) CE and (i) BNR are shown for different values of the analysis kernel size n in the coronal (○) and transverse (▲) direction. For inversion recovery with on-resonant water suppression (IRON) as a function of the pre-pulse bandwidth, the (i) volume of enhancement, (j) PC, (k) CE, and (l) BNR are shown for gradient echo (○ and ▲) and fast spin echo (● and Δ) in coronal and transverse plane, respectively. Next, for fast low angle SSFP (FLAPS) as a function of the flip angle, (m) the volume, (n) PC, (o) CE, and (p) BNR are plotted for acquisitions in the (○) coronal and transverse (▲) plane. Measures of positive contrast for the iterative decomposition of water and fat with echo asymmetry and least-squares estimation (IDEAL) method calculated from a echo-time series of $\Delta TE=1.0$ ms (for off resonance 333 Hz), 2.3 ms (~145 Hz) and 5.8 ms (~57 Hz) are shown, with (u) the volume, (v) PC, (w) CE and (x) CNR in the coronal (○) and (▲) transverse plane. For 145 Hz the measurement bandwidth was larger, due to gradient limitations, and that for 333 Hz, separate acquisitions instead of a multi-echo scan was used.

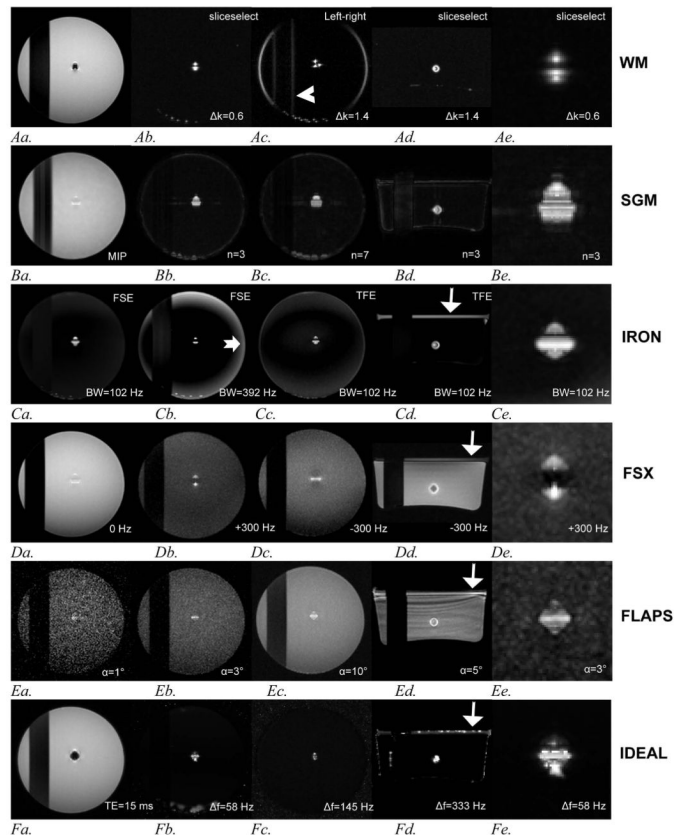


Fig 6. Composition of images from the different methods. (Aa) White marker (WM) center slice of non-dephased image (Ab) 21-slice MIP with dephasing $+0.6 \cdot k_{\max}$ in slice-select direction (Ac) dephasing in fold-over direction of $1.4 \cdot k_{\max}$. Enhancement in regions of signal changes in the native image can be seen (white arrowhead). (Ad) axial MIP $+1.4 \cdot k_{\max}$ in slice-select (Ae) 4x zoom 21-slice MIP coronal $+0.6 \cdot k_{\max}$ dephasing in slice-select (Ba) MIP of source images for SGM, (Bb) SGM with kernel size 3 and (Bc) 7, (Bd) axial image for kernel size 3 (Be) 4x zoomed MIP kernel size 3. (Ca) coronal MIP IRON FSE BW=102 Hz and (Cb) 392 Hz. A rim of residual signal is seen at the phantoms edge (short arrow). (Cc) TFE IRON BW=102 Hz (coronal) (Cd) axial TFE MIP BW=102 Hz showing fat layer on top (white arrow) (Ce) 4x zoomed MIP TFE BW=102 Hz. (Da) Frequency selective excitation (FSX) with 0 Hz detuning (Db) +300 Hz and (Dc) -300 Hz detuning. (Dd) -200 Hz detuning axial orientation (fat shows at white arrow) (De) zoomed MIP +300 Hz detuning. (Ea) FLAPS image for flip angle $\alpha=1^\circ$, (Eb) $\alpha=3^\circ$ (Ec) $\alpha=10^\circ$, (Ed) axial FLAPS image for $\alpha=5^\circ$ (white arrow shows fat), (Ee) zoomed MIP for $\alpha=3^\circ$. (Fa) IDEAL source image TE=14.8 ms (Fb) IDEAL off resonance image $\Delta f=58$ Hz and (Fc) $\Delta f=145$ Hz, (Fd) axial off resonance $\Delta f=333$ Hz (fat shown at arrow) (Fe) zoomed MIP $\Delta f=58$ Hz.

Table 1

Categories into which the 6 methods investigated can be divided. White Marker (WM) can both be implemented using modified acquisition as well as a post-processing method (see also (32)). The other methods are: inversion recovery with on-resonant water suppression (IRON), frequency selective excitation (FSX), and closely related to the frequency based methods: fast low flip-angle positive contrast SSFP (FLAPS), and iterative decomposition of water and fat with echo asymmetry and least-squares estimation (IDEAL).

	Acquisition	Post-processing
K-space based	WM	SGM WM
Frequency based	IRON FSX	
Phase accumulation based	FLAPS	IDEAL

General properties of the different methods. Listed are the sensitivity to the quality of the acquisition shimming, the sensitivity to RF(B₁) inhomogeneities, the possible appearance of fat in the positive contrast images, the possibility to accelerate image acquisition (relative to cardiac triggered scanning), the possibility to select the relative amount of background suppression and a few specific properties, which may influence application.

Table 2

<i>Technique</i>	<i>Shimming sensitivity</i>	<i>RF homogeneity sensitivity</i>	<i>Background inhomogeneity</i>	<i>Fat signal</i>	<i>Acquisition speedup</i>	<i>Flexible suppression</i>	<i>Realtime capability</i>	<i>Other</i>
WM/GRASP	Little, Correct F0 important for stability of contrast	no	Sensitive to partial volume effects and local signal intensity changes in the direction of the dephasing	None, except at the interface where the signal changes	Comparable to regular imaging, with some limitations to sequence. Can be steady state acquisition.	Yes, but relatively narrow optimum for good CNR	Yes,	Possible as postprocessing method (then output resolution is lowered).
IRON	Yes, required accuracy related to bandwidth of the prepulse	Yes, the flipangle of the prepulse determines contrast	Little, T1 dependent	Yes, fatsat needed	Read-out can be fast, but prepulse requires time	Yes	Yes, temporal resolution depends on suppression bandwidth	Can be combined with any imaging sequence, e.g. spin echo.
SGM	Little, but proportional to kernel size.	no	Less than WM/GRASP	None	(Post-processing method). Some limitations to acquisition.	No, only through blending with source image	No, requires post-processing	Output resolution lower
FSX	Yes, related to bandwidth of excitation	Little, only intensity variations	none	Yes, Dependent on frequency offset, using fatsat	Allows steady state acquisition.	Yes	Yes	Visualizes either negative or positive frequency shifts
FLAPS	Very, banding-artefacts can occur	Yes, contrast determined by effective flip angle	Strong background signal, depending on T1/T2.	Yes, fatsat needed	Very fast. Allows steady state acquisition.	No, only through flip-angle controls (contrast).	Yes	

<i>Technique</i>	<i>Shimming sensitivity</i>	<i>RF homogeneity sensitivity</i>	<i>Background inhomogeneity</i>	<i>Fat signal</i>	<i>Acquisition speedup</i>	<i>Flexible suppression</i>	<i>Realtime capability</i>	<i>Other</i>
IDEAL	Little, the method incorporates a field map	no	none	Yes, dependent on frequency spacing, fatsat needed	(Post-processing method). Requires multi-echo data.	Yes (by choosing frequency spacing and offset)	No, requires post-processing	On- and off-resonance images, T2* and a phasemap, sensitive to noise